Theranostic Activity of Ceria-Based Nanoparticles toward Parental and Metastatic Melanoma: 2D *vs* 3D Models

Kochurani K. Johnson,* Chantal Kopecky, Pramod Koshy, Yiling Liu, Michelle Devadason, Jeff Holst, Kristopher A. Kilian, and Charles C. Sorrell

Cite This: *ACS Biomater. Sci. Eng.* 2023, 9, 1053−1065

Read Online

| ACCESS | | Metrics & More | | Article Recommendations | | Supporting Information |

ABSTRACT: The time interval between the diagnosis of tumor in a patient and the initiation of treatment plays a key role in determining the survival rates. Consequently, theranostics, which is a combination of diagnosis and treatment, can be expected to improve survival rates. Early detection and immediate treatment initiation are particularly important in the management of melanoma, where survival rates decrease considerably after metastasis. The present work reports for the first time the application of fluorescein isothiocyanate (FITC)-tagged epidermal growth factor receptor (EGFR)-functionalized ceria nanoparticles, which exhibit intrinsic reactive oxygen species (ROS)-mediated anticancer effects, for the EGFR-targeted diagnosis and treatment of melanoma. The theranostic activity was demonstrated using two-dimensional (2D) and three-dimensional (3D) models of parental and metastatic melanoma. Confocal imaging studies confirm the diagnostic activity of the system. The therapeutic efficiency was evaluated using cell viability studies and ROS measurements. The ROS elevation levels are compared across the 2D and 3D models. Significant enhancement in the generation of cellular ROS and absence in mitochondrial ROS are observed in the 2D models. In contrast, significant elevations in both ROS types are observed for the 3D models, which are significantly higher for the metastatic spheroids than the parental spheroids, thus indicating the suitability of this nanoformulation for the treatment of metastatic melanoma.

KEYWORDS: *cancer theranostics, nanoceria rods, parental and metastatic melanoma, 2D and 3D cancer models, EGF and EGFR*
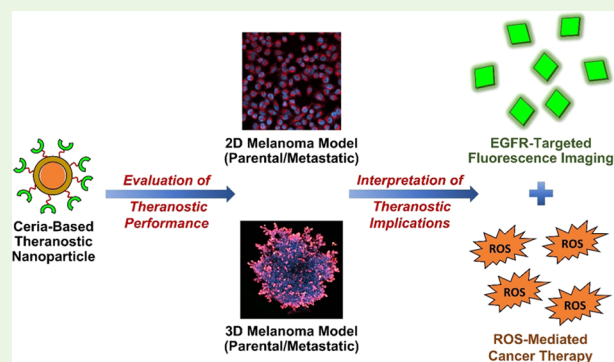
1. INTRODUCTION

The time lapse between the tumor diagnosis and the initiation of cancer treatment is a critical factor that determines the survival rate of a patient.[1] Therefore, it is important to minimize the associated time interval. Theranostics offers the advantage of combining diagnostic strategies and therapeutic strategies into one single system,[2] so this combination can be effective in minimizing this time period by combining the multiple stages of diagnosis and treatment into a single stage. This approach also can provide improved molecular-level understanding of the disease while allowing tailored treatment based on the therapeutic needs of the patient.[3]

When nanoparticles are employed to deliver diagnostic and therapeutic agents to tumor sites, such nanotheranostic systems offer significant potential for nanoscale engineering and formulation. This approach also can allow the simultaneous loading of several diagnostic agents and anticancer agents onto the same theranostic nanoparticles. Consequently, these multimodal theranostic systems offer the benefits of multiple diagnostic and therapeutic strategies.[4] Further, nanoparticles with intrinsic diagnostic and/or therapeutic properties can be incorporated as an intrinsic feature of the

system. Since nanoceria exhibits intrinsic anticancer properties[5−8] and has been employed for the therapeutic management of cancer, the present work aims at exploring the potential for nanoceria as the therapeutic component of the theranostic system. A diagnostic component, which is a fluorophore-tagged ligand that is targeted at the epidermal growth factor receptor (EGFR), is conjugated with nanoceria to formulate the theranostic agent.

The therapeutic activity of nanoceria is highly tumor-specific as its anticancer activity is triggered by the pH of the medium. Cerium exists in two oxidation states, Ce^{3+} and Ce^{4+}, and can switch between these states based on the pH.[9] This characteristic feature enables it to act as a pro-oxidant in acidic pH, thus elevating the production of reactive oxygen species (ROS), and as an antioxidant in basic pH, thus
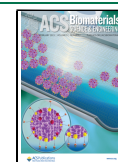
scavenging the ROS. Consequently, the acidic pH levels of cancer cells facilitate the killing of tumor cells while the basic pH levels of normal cells facilitated the protection of healthy cells.[10] The elevation of the ROS levels in tumor cells subjects them to excessive oxidative stress, eventually leading to the tumor cell death by ROS-mediated autophagy, necrosis, and apoptosis.[11,12] One major advantage of employing nanoceria for the management of cancer is its negligible or minimal side effects on healthy cells.[5] This well-known advantage is attributed to the ability of nanoceria to mimic the enzymes superoxide dismutase (SOD) and catalase (CAT).[5] The cytoprotective and cytotoxic behavior depends on the pH of the media, where the former is active in physiological pH (7.4) and the latter is active in the tumor microenvironment pH (6.4).[9] The enzymatic activity associated with the former results in the neutralization of the ROS superoxide and hydrogen peroxide, thereby protecting healthy cells from the cytotoxic effects of these ROS. This pH-based cytoprotection offers the potential to overcome the main challenge associated with the management of cancer, which is the toxic side effect of anticancer agents.[13−16]

Receptor-targeted imaging of tumors is a promising approach for the diagnosis of cancer.[17] The most important class of cancer biomarkers is receptors, and this serves not only as diagnostic biomarkers but also as prognostic and predictive biomarkers in the management of cancer.[18] There are several receptors overexpressed in different types of cancers, such as G-protein-coupled receptors (GPCRs),[19] integrins,[20] epidermal growth factor receptors (EGFRs),[21] and folate receptors (FRs).[22] The selection of ligands that can be used as functionalization agents to target the receptors depends entirely upon the receptor to be targeted. Natural ligands of receptors are excellent targeting agents owing to their high affinity for target receptors.[23] These ligands can be conjugated with imaging agents and used as diagnostic agents.[17] Fluorescent probes based on fluorescein isothiocyanate (FITC),[24] cyanine dyes,[25] boron dipyrrole carbinol difluoride dyes (BODIPY),[26] rhodamine,[27] and other dyes are excellent imaging agents that can be employed for receptor-targeted imaging of tumors.[28] Apart from providing the diagnosis of tumors, receptor-targeted imaging also can aid in the assessment of surgical margins during the excision of tumor and can predict the presence of metastatic lymph nodes.[29] Further, functionalization of nanoparticles with a receptor-targeted ligand enables the tumor-specific delivery of anticancer agents, thereby enhancing the bioavailability of therapeutic drugs at the tumor site and avoiding side effects.[1]

The potential for receptor-targeted imaging represents an attractive and promising aspect of nanotheranostics. Several receptor-targeted imaging modalities have been employed previously in the theranostic imaging of some cancers.[30,31] These modalities include imaging strategies, including optical imaging,[32,33] nuclear imaging,[34] ultrasound imaging,[35] and magnetic resonance imaging (MRI) imaging.[36] Of these, receptor-targeted fluorescence imaging has emerged as the principal strategy for the diagnosis of different cancers, including breast cancer,[37] glioma,[38] lung cancer,[39] ovarian cancer,[40] and melanoma.[41]

Melanoma, the most aggressive type of skin cancer,[42] has experienced a global increase of occurrence over the last decade, with 324,625 cases diagnosed in 2020.[43] When detected in its early stages, it is possible to treat successfully, thereby offering high survival rates for patients; survival rates

decrease considerably after tumor metastasis.[44] Therefore, the successful management of melanoma requires early tumor diagnosis and immediate treatment. Initial misdiagnosis of melanoma is another factor that can reduce the survival rates of melanoma patients.[45] While there has been an increase in the number and scope of new drugs, particularly for targeted therapies, the rapidly emerging resistance to such treatments is a key challenge yet to be overcome.[46] Therefore, it is critical to develop superior targeted therapies for the successful treatment of melanoma. It also is critical to provide early diagnosis and immediate treatment in the management of melanoma, where theranostics can provide effective solutions by integrating these multiple steps into one.

EGFR is an important biomarker for an array of tumors[47] and can act as a promising target for the diagnosis and treatment of melanoma, especially in metastatic melanoma,[48] revealing the potential of EGFR-targeted theranostics in melanoma management. In the present work, fluorophore-tagged EGF was used as the diagnostic component and nanoceria was used as the therapeutic component. The EGFR-positive cell line A375[49] was selected for the targeting study. To evaluate the theranostic performance of the system on parental and metastatic cell lines, the poorly metastatic cell line A375-P[50] and a more metastatic cell line A375-MA1[51] were used. The theranostic performance also was contrasted between two-dimensional (2D) and three-dimensional (3D) melanoma models rather than by in vivo testing. The latter has emerged as a standard drug-testing system that can replace animal models in many aspects of preclinical testing.[52] 3D models were included in the study to overcome the limitations of the 2D models, which include alteration of cell phenotype, polarity, and mode of division.[53] The 3D spheroidal microstructures are more representative of actual tumor masses and other in vivo conditions, such as cell−cell and cell−environment interactions.

Although previous works have reported the ROS-mediated anticancer effects of nanoceria[9,54] and the potential for EGFR targeting using other nanoparticle-based systems,[55−57] the present work appears to be the first to report the potential for EGFR-targeted theranostic applications of EGF-functionalized nanoceria. This novel attempt to functionalize nanoceria with EGF for theranostic applications can assist in enhancing the bioavailability of nanoparticles at the tumor site through receptor-mediated endocytosis of the particles, allowing both imaging and treatment of cancer. Since EGF is a natural protein, the process also can improve the nanoparticles' biocompatibility, which appears to be the most critical factor in the successful clinical translation of nanomedicines.

In summary, the present work reports the investigation of the performance of a nanoparticulate system on melanoma, as shown in Figure 1. To these ends, EGF, the natural ligand of the EGFR receptor, tagged with fluorescein isothiocyanate (FITC) as a fluorescent probe was employed as a diagnostic agent. This was conjugated with nanoceria as a therapeutic agent to formulate the theranostic agent. Specifically, the data evaluate the theranostic performance of a fluorophore-tagged, EGFR-targeted, ceria-nanorod-based theranostic formulation on parental (A375-P) and metastatic (A375-MA1) melanoma using 2D and 3D melanoma models.

2. EXPERIMENTAL SECTION

2.1. Materials. Cell Counting Kit 8 (CCK-8), 2′,7′-dichlorodihydrofluorescein diacetate (DCFH-DA), and 4′,6-diamidino-2-phenyl-
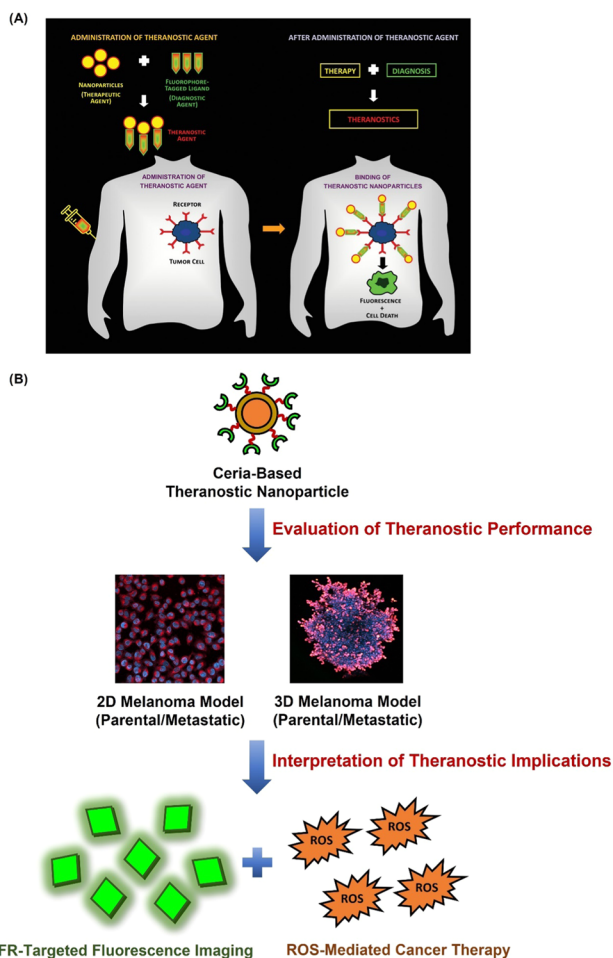
Figure 1. (A) Overview of receptor-targeted theranostics. Reproduced with permission from ref 1. Copyright 2021 Wiley. (B) EGFR-targeted theranostics in 2D and 3D melanoma models.

indole (DAPI) were purchased from Sigma-Aldrich, Australia. Nitric acid was purchased from RCI Labscan Limited, Australia. Dulbecco's modified Eagle's medium (DMEM), penicillin–streptomycin solution, trypsin-ethylenediaminetetraacetic acid (EDTA), Dulbecco's phosphate-buffered saline (DPBS), Hank's balanced salt solution (HBSS), fetal bovine serum (FBS), MitoSox, Triton X-100, Vybrant DiD cell-labeling solution, Hoechst 33342 solution, live/dead viability/cytotoxicity kit (calcein AM and ethidium homodimer-1 (EthD-1)), and 16% w/v paraformaldehyde (PFA; methanol-free) were purchased from Thermo Fischer Scientific, Australia. A375-P and A375-MA1 cell lines were purchased from American Type Cell Culture (ATCC).

2.2. Characterization of Theranostic Nanoparticles. The mineralogical, morphological, structural, particuological, and chemical characterization of nanoceria was performed as described elsewhere.[58] Dynamic light scattering (DLS; Malvern Zetasizer Nano ZS, U.K.; 10 mW, 633 nm He–Ne laser) analyses of nonfunctionalized nanoceria ((3-aminopropyl)triethoxysilane (APTES)-nanoceria) and the final theranostic nanoformulation were performed to determine the hydrodynamic size distributions and the ζ potentials. The aqueous suspensions were sonicated 8 min prior to analysis.

2.3. Cell Culture. Human parental (A375-P) and metastatic (A375-MA1) melanoma cells were cultured in DMEM, supplemented with 10 vol % FBS and 1 vol % penicillin–streptomycin, and incubated at 37 °C under 5 vol % CO_2.

2.4. Cell Viability Assay. A375-P and A375-MA1 cells were seeded in three 96-well plates at a seeding density of 2000 cells/well and incubated for 24 h. The medium was removed and replaced with 100 μL of fresh DMEM in the control wells and with 100 μL of

FITC-tagged EGF-nanoceria in the test wells at 200 μg/mL concentration. Six wells per test were used. Each plate was then incubated for 24, 48, or 72 h. After the respective incubation periods, CCK-8 reagent (10 μL) was added to each well, incubated for 3 h, and the optical absorbance (CLARIOstar plus, BMG LABTECH, Germany) at 450 nm was measured.

2.5. Measurement of ROS Production in 2D Models. ROS generation levels in cancer cells were measured using two ROS-detection assays: DCFDA assay and MitoSOX assay. A375-P and A375-MA1 cells were seeded as described immediately above and treated with 200 μg/mL of nanoparticles and incubated for 48 h. The cells were washed with 1× DPBS, and then 1× trypsin (100 μL) was added to each well. Each plate was incubated for 5 min, and then DCFH-DA in HBSS (10 μM) and MitoSOX in HBSS (10 μM) were added to the respective plates to achieve a final concentration of 5 μM, followed by incubation for 40 min. The fluorescence intensities at 485/535 and 510/580 nm were then determined. As demonstrated in previous work by the authors,[58] EGF functionalization improves the ROS-mediated anticancer activity as well as the overall therapeutic performance relative to nonfunctionalized nanoceria. Consequently, the latter was not examined as a control for the cytotoxicity evaluation in 2D and 3D models.

2.6. Quantification of Cellular Uptake of Nanoceria Using ICP-MS. A375-P and A375-MA1 cells were seeded in 24-well plates at a seeding density of 4000 cells/well and incubated for 24 h. The RPMI in the wells was replaced with 200 μg/mL of theranostic nanoparticles and incubated for 48 h. Three wells per test were used. After the incubation time, nanoparticles were discarded, and the cells were washed thrice with 1× DPBS. Trypsin (500 μL) was added, and each plate was incubated for 5 min. Trypsinized cells were then digested completely using concentrated nitric acid. The cerium content in each sample was quantified using inductively coupled plasma mass spectrometry (ICP-MS; PerkinElmer quadrupole NexION) using a standard cerium solution. Untreated cells were processed in the exact same way as mentioned above and were used as controls for quantification.

2.7. Imaging of Cellular Uptake of Nanoparticles in 2D Models Using Confocal Microscopy. For confocal imaging studies, A375-P and A375-MA1 cells were seeded in 96-well glass-bottom plates at a seeding density of 10,000 cells/well and incubated for 24 h. Triplicate wells were used for each test. After 24 h of incubation, the medium in each well was replaced with 200 μg/mL nanoparticles and each plate was incubated for 30 min. After incubation, the cells were washed three times with 1× DPBS and stained with the cell membrane dye (Vybrant DiD diluted in a ratio of 1:200 using DMEM media). Staining was performed at 37 °C for 20 min, after which the cells were washed thrice with 1× DPBS and fixed by 4% (w/v) PFA for 15 min at room temperature. The cells were then washed thrice and treated with a permeabilization agent (0.1% Triton X-100) for 15 min at room temperature. The cells were then washed thrice with 1× DPBS, and then DAPI diluted with 1× DPBS in a 1:500 ratio was added and incubated for 20 min at room temperature. The cells were washed thrice and imaged using confocal laser scanning microscopy (Zeiss LSM 800, Germany) using a 20× objective (Plan-Apochromat 20×/0.8 M27, 640 nm/0.71 au, 488 nm/0.80 au, 405 nm/1.00 au) and a 63× objective (Plan-Apochromat 63×/1.40 Oil DIC M27, 640 nm/0.52 au, 488 nm/0.58 au, 405 nm/0.73 au).

2.8. Formation of 3D Spheroids. A375-P and A375-MA1 cells, grown as monolayer cultures, were trypsinized and seeded in 96-well, round-bottom, ultralow-attachment plates at a seeding density of 2000 cells/well, and each plate was centrifuged at 380g for 3 min at room temperature. The centrifugation ensured the uniform clustering of all of the seeded cells within the wells, which then enabled the formation of the spheroids. The plate was then incubated for 72 h to facilitate the formation of spheroids that were used for further testing.

2.9. Measurement of ROS Production in 3D Models. ROS generation levels in parental and metastatic spheroids were measured using the DCFDA assay and MitoSOX assay. A375-P and A375-MA1 spheroids were generated as described immediately above and treated
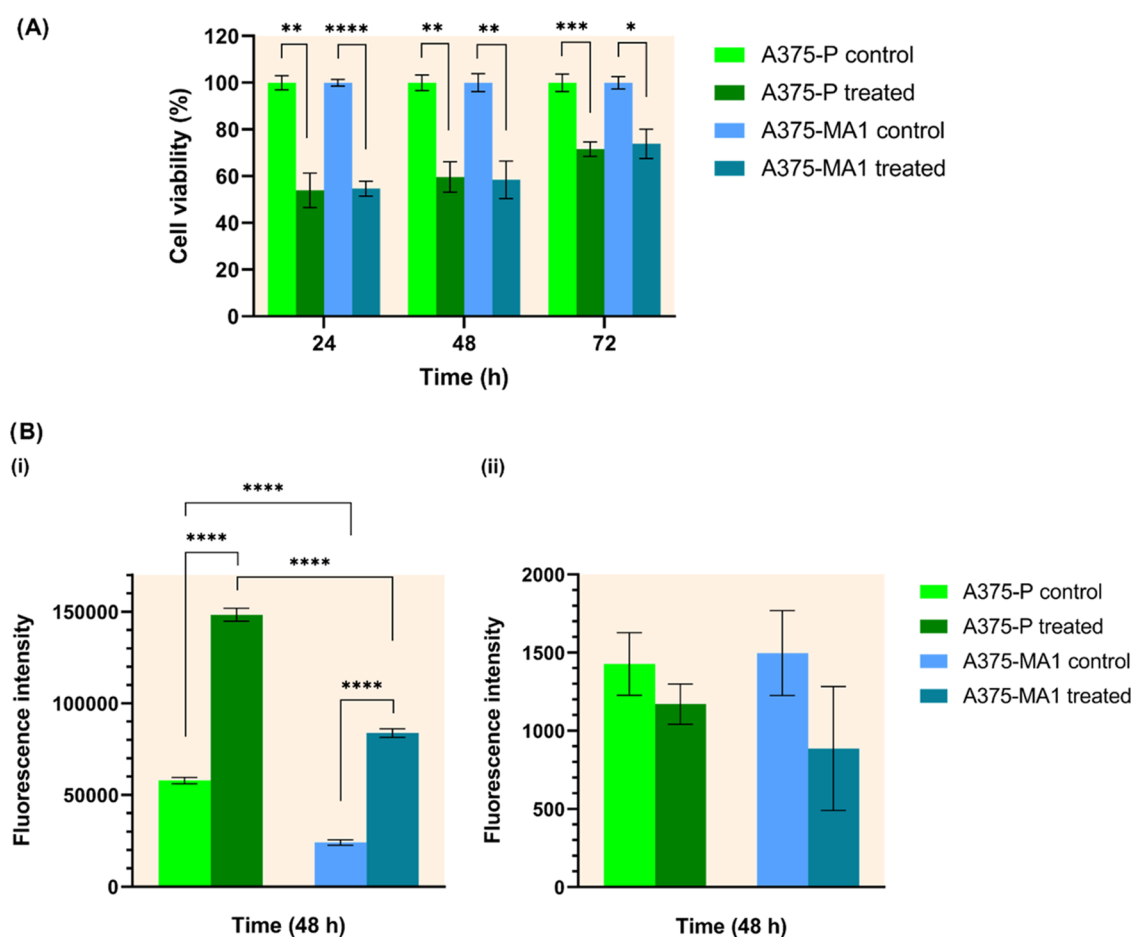
Figure 2. Therapeutic activity of nanoparticles on 2D models. (A) Viability of A375 cells treated with nanoparticles. (B) ROS generation levels in melanoma cell lines treated with nanoparticles at 48 h: (i) DCFDA assay, (ii) MitoSOX assay.

with 200 μg/mL nanoparticles and incubated for 48 h. The cells were washed twice with 1× DPBS and resuspended in 100 μL of 1× DPBS. DCFH-DA (100 μL) in HBSS (10 μM) and MitoSOX in HBSS (10 μM) were added to the spheroids to achieve a final concentration of 5 μM, followed by incubation for 1 h. The fluorescence intensities at 485/535 and 510/580 nm were then determined. This tenure was selected to achieve sufficient reagent penetration in the spheroids; the reduced time of 40 min in the case of the 2D model, which is a monolayer, was sufficient to achieve the same outcome.

2.10. Live/Dead Imaging of Nanoparticle-Treated 3D Spheroids Using Confocal Microscopy. A375-P and A375-MA1 spheroids were generated in 96-well, round-bottom, ultralow-attachment plates, as mentioned previously. The medium in each well was replaced with 200 μg/mL nonfluorescent EGF-nanoceria, and the plates were incubated for 48 h. After incubation, the spheroids were washed twice with 1× DPBS. Live and dead cell staining mix (200 μL) consisting of 2 μM calcein AM and 4 μM ethidium homodimer-1 (EthD-1) were added to the spheroids, followed by incubation for 30 min. The spheroids were washed twice with 1× DPBS, transferred quickly to 96-well glass-bottom plates, and imaged using confocal laser scanning microscopy (Zeiss LSM 800, Germany) using a 10× objective (Plan-Apochromat 10×/0.45 M27, 561 nm/0.83 au, 488 nm/1.00 au).

2.11. Imaging of Cellular Uptake of Nanoparticles in 3D Models Using Confocal Microscopy. A375-P and A375-MA1 cells were seeded in 96-well, round-bottom, ultralow-attachment plates for the generation of spheroids. Triplicate wells were used for each test. After the formation of spheroids, the medium in each well was replaced with 200 μg/mL nanoparticles, and the plates were incubated for 30 min, 1 h, or 2 h. After the respective incubation periods, the spheroids were washed twice with 1× DPBS and co-

stained with the cell membrane dye (Vybrant DiD and Hoechst 33342 DNA stain). Vybrant DiD was diluted in the ratio of 1:200 using DMEM, and Hoechst 33342 DNA stain was diluted in the ratio of 1:1000 using DMEM. The co-staining was done by incubation for 1 h at 37 °C. The spheroids were then washed with 1× DPBS thrice by gently replacing the DPBS in the well each time, followed finally by fixing with 4% (w/v) PFA for 24 h at room temperature while shaking the plate. The fixed spheroids were washed four more times with 1× DPBS, transferred to 96-well glass-bottom plates, and imaged using confocal laser scanning microscopy (Zeiss LSM 800, Germany) using a 10× objective (Plan-Apochromat 10×/0.45 M27, 640 nm/0.64 au, 488 nm/0.72 au, 405 nm/1.00 au).

2.12. Statistical Analysis. The statistical analyses were done using GraphPad Prism software, and the data are given as a function of mean and standard error of the mean (SEM; error bars). The testing included one-way analysis of variance (ANOVA) or two-way analysis of variance; P values <0.05 were considered statistically significant: *$P \leq 0.05$, **$P \leq 0.01$, ***$P \leq 0.001$, and ****$P \leq 0.0001$.

3. RESULTS AND DISCUSSION

3.1. Characterization of Nanoparticles. Characterization of the mineralogical, morphological, structural, and chemical properties of nanoceria also was performed, as described globally in the authors' previous work.[58] The size of the hydrothermally synthesized ceria nanorods was 83.9 ± 27.3 nm length and 12.4 ± 1.6 nm diameter/width, as measured by transmission electron microscopy (TEM) imaging. The hydrodynamic diameter data for the APTES-nanoceria and
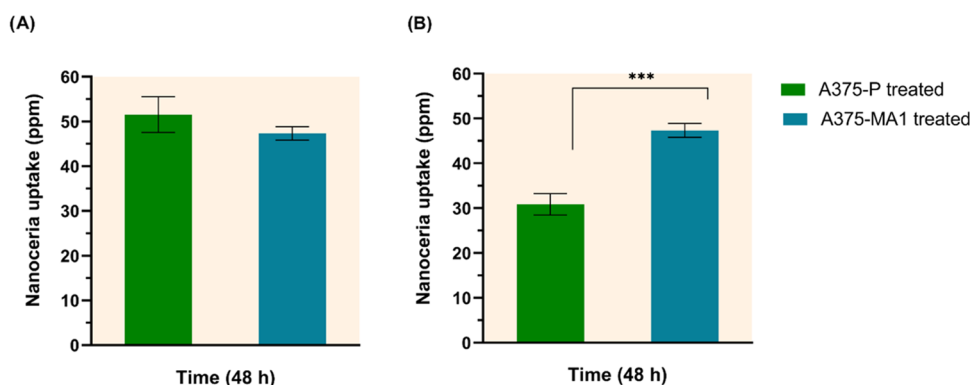
Figure 3. Cellular uptake levels of nanoparticles by parental and metastatic A375 cells measured by ICP-MS: (A) observed uptake levels, (B) normalized uptake levels.

FITC-EGF-nanoceria are shown in Figure S1 (Supporting Information), and they are summarized in Table S1 (Supporting Information). The ζ potentials for the two nanoceria were +15 and −28 mV, respectively.

The normal distribution of the APTES-nanoceria, with an average of ∼120 nm indicates that homogeneously sized agglomerates formed from the nanoceria rods of length ∼50 and ∼12 nm width. The TEM data indicate that these agglomerates consisted of aligned nanorods that share prism facets. The positive ζ potential of +15 mV is consistent with the tendency to agglomerate, *viz.*, <30 mV[59] and a positive surface charge of APTES at pH 7.[60] In contrast, the FITC-EGF-nanoceria exhibits three scales of agglomerates. The small agglomerates (∼120 nm) show that they are soft agglomerates as these are smaller than the base APTES-nanoceria. The medium agglomerates (∼435 nm) suggest that the functionalization enhances the tendency to form larger soft agglomerates. The negative ζ potential of −28 mV again is consistent with the tendency to agglomerate but with a negative value consistent with that of EGF at pH 7.[61] The small population of large agglomerates (∼5100 nm) is likely to derive from the presence of a very few agglomerated agglomerates (these data are volumetric).

3.2. Therapeutic Potential for Theranostic Nanoparticles in 2D Models. The therapeutic activities of theranostic nanoparticles in parental and metastatic 2D models were determined by cell viability tests done at 24, 48, and 72 h post-treatment. The results shown in Figure 2A demonstrate that the nanoceria-induced percentages of tumor cell death were statistically indistinguishable for both parental and metastatic cell lines at each time point. The respective percentages for cell viability for A375-P and A375-MA1 were 54 ± 8 and 55 ± 3% at 24 h, 60 ± 6 and 58 ± 9% at 48 h, and 72 ± 4 and 74 ± 6% at 72 h, respectively. These data reveal similar therapeutic activities of EGFR-targeted nanoceria in both of the 2D models, despite the expected increased levels of EGFR expression in more metastatic melanoma.[48,62] The reason for this observation, which is the limitations of the 2D models, is discussed subsequently in Section 3.8.

The average viabilities of the melanoma cells increased with time, although the first two time points are statistically indistinguishable. As shown by the nonoverlap of the error bars, a significant increase in viability is observed for the last time point studied (72 h), thereby suggesting a decrease in the generation of ROS. This trend is attributed to the blockage of catalytically active sites of nanoceria[63−66] by the accumulation of cell debris, generated from cell death,[67,68] thereby hindering ROS generation.

Since the therapeutic performance of nanoceria is related directly to its ability to raise the ROS to cytotoxic levels in tumor cells,[69,70] the ROS generation levels in A375-P and A375-MA1 cells treated with nanoparticles at 48 h were measured. Figure 2B shows these ROS levels, as detected by the DCFDA assay and MitoSox assay. These assays detect the generation of different ROS: DCFDA detects the cellular generation of hydrogen peroxide (H_2O_2) and hydroxyl ($^\bullet OH$), whereas MitoSOX detects the mitochondrial generation of superoxide ($^\bullet O_2^-$).[9] The DCFDA assay reveals significant ROS-induced oxidative stress on both of the treated cell lines compared to their controls (fluorescence intensity range to 150,000). Hence, the organelles within the cells are vulnerable to the catalytic effects of nanoceria in the 2D models. It also can be seen that the cellular ROS generation levels are higher for the parental cell line. However, the latter data are mitigated because, although the seeding densities were the same for both cell lines, the growth rates are not the same. Hence, the relative trends reflect the effect of increasing cell numbers and the corresponding increasing ROS generation levels. These data show that the cellular oxidative stress induced by the nanoparticles is significant, thus revealing the therapeutic potential for nanoceria in melanoma therapy.

In contrast, the mitochondrial ROS generation levels as detected by the MitoSOX assay are significantly lower (fluorescence intensity range to 1500, which is similar to that of the blank) and the differences between the treated cell lines compared to their controls are statistically indistinguishable. Hence, the mitochondria within the cells appear not to be vulnerable to the catalytic effects of nanoceria in the 2D models. Although the average values of these data suggest the possibility of a cytoprotective effect, this is extremely unlikely as ceria is cytotoxic. As will be discussed subsequently in Section 3.8, these trends are not supported by the 3D models, thereby confirming the limitations of the 2D models.

3.3. Cellular Uptake Levels of Theranostic Nanoparticles in Parental and Metastatic 2D Models. The cellular uptake levels of nanoceria were compared across the parental and metastatic cell lines, as shown in Figure 3. The raw measurements by ICP-MS of the uptake levels show no significant differences between the two cell lines (Figure 3A). However, as the growth rates of these two cell lines differ, the normalized data (on the basis of the metastatic cell count) reveal a significant difference, as summarized in Table S2
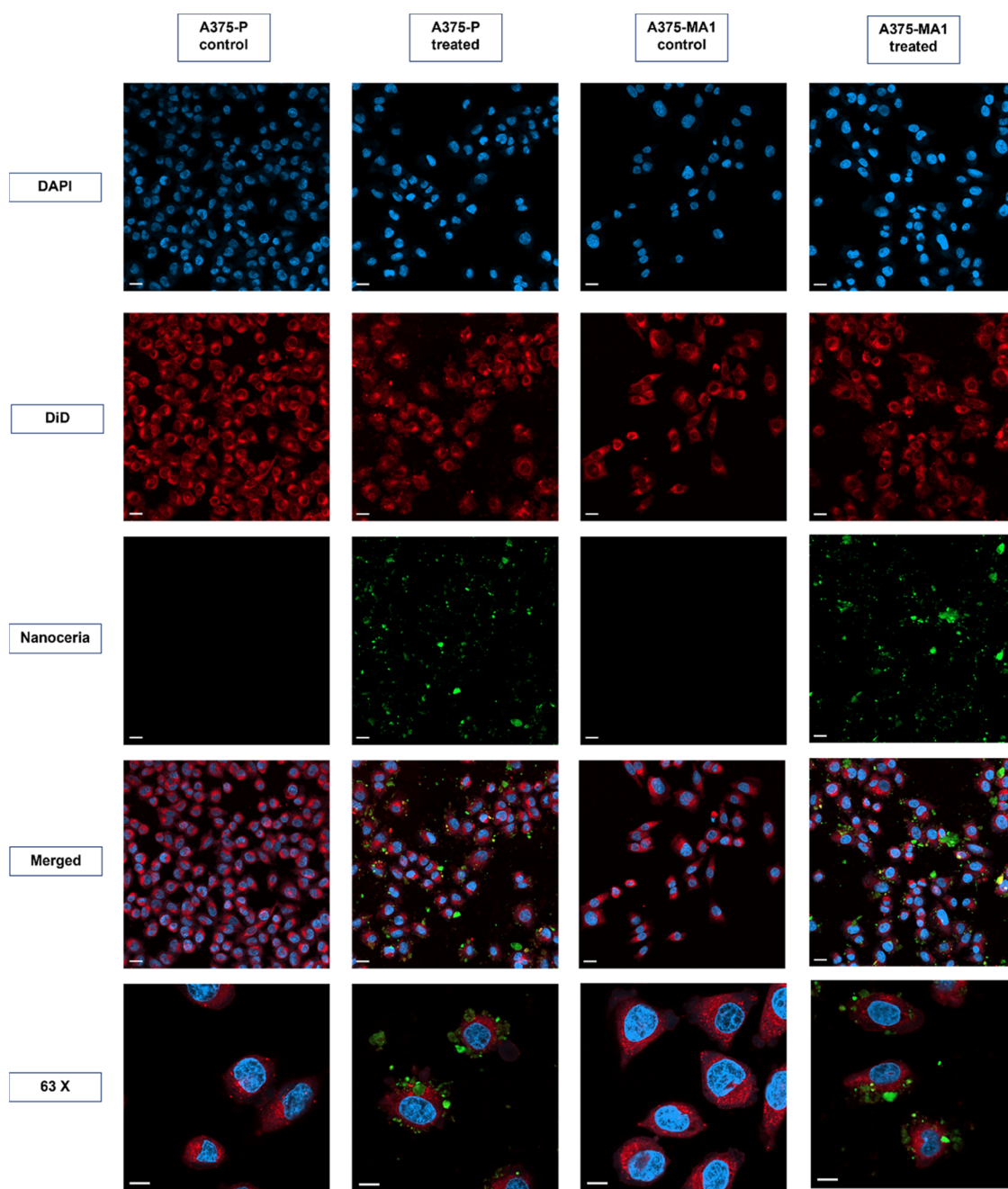
Figure 4. Confocal imaging of melanoma cells after 30 min of treatment with EGFR-targeted nanoparticles (scale bar: 20 μm [20×] and 10 μm [63×]).

(Supporting Information). These data show that the uptake level of the nanoparticle by the metastatic cells was >50% higher than that of the parental cells. This is attributed to the higher levels of EGFR expression in the metastatic cells, which facilitated the higher rate of uptake by EGFR-mediated endocytosis of nanoparticles.

3.4. Diagnostic Potential for Theranostic Nanoparticles in 2D Models. The diagnostic activities of the nanoparticles were demonstrated by treating the melanoma cells with theranostic nanoparticles and their subsequent imaging using confocal microscopy. As the cell lines used in this study were EGFR-positive, the entry mode of theranostic nanoparticles into the cells is attributed to receptor-mediated endocytosis,[71] where the nanoparticles are functionalized with

EGF (FITC-tagged), which is a high-affinity ligand of EGFR.[72] The cells were imaged after 30 min of treatment with the nanoparticles, where the nanoparticles are seen in Figure 4 to be in contact with the cells or partially taken up by the cells, as indicated by their proximity to the cell surfaces. The magnified images at 63× (bottom row) confirm this. As demonstrated in previous work by the authors,[58] the interaction of EGF-functionalized nanoparticles with EGFR facilitates the internalization of the nanoparticles. This is attributed to clathrin-mediated endocytosis, where the receptor is first recruited to clathrin-coated pits, followed by its internalization.[73]

3.5. Formation of 3D Spheroids. Figure S2 (Supporting Information) shows the melanoma spheroids of parental and metastatic cell lines on day 6 of the seeding, although the
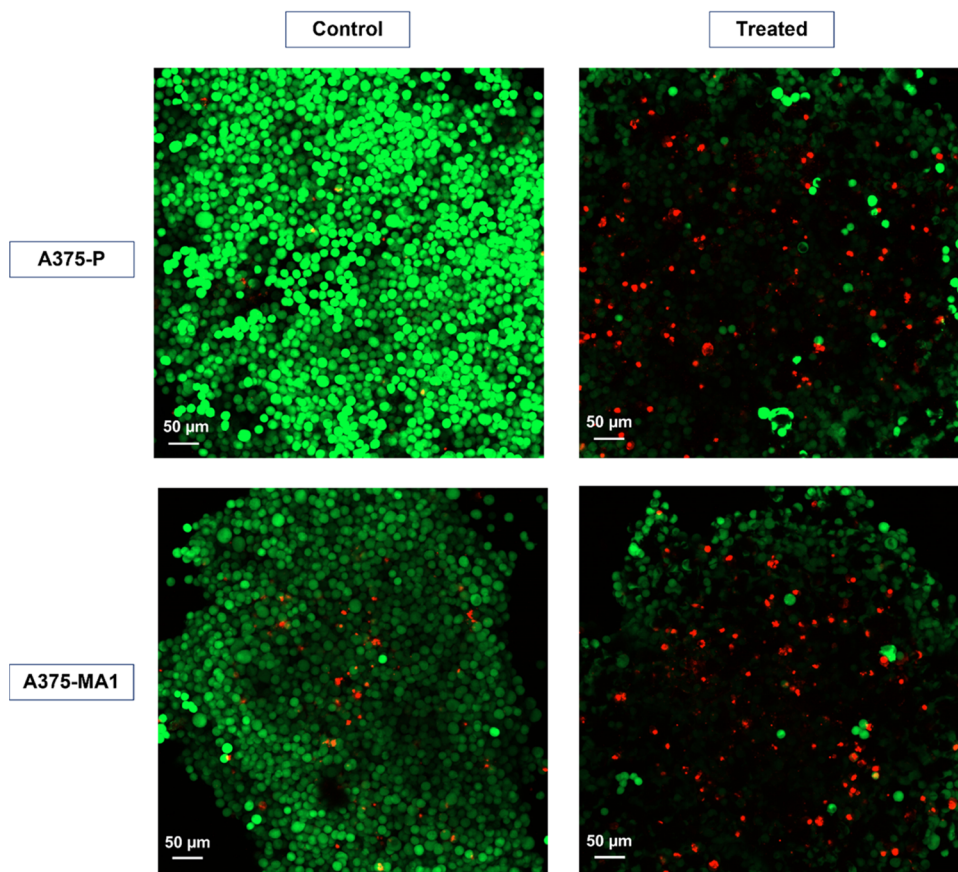
Figure 5. Live/dead staining and subsequent imaging of melanoma 3D models treated with nanoparticles for 48 h.
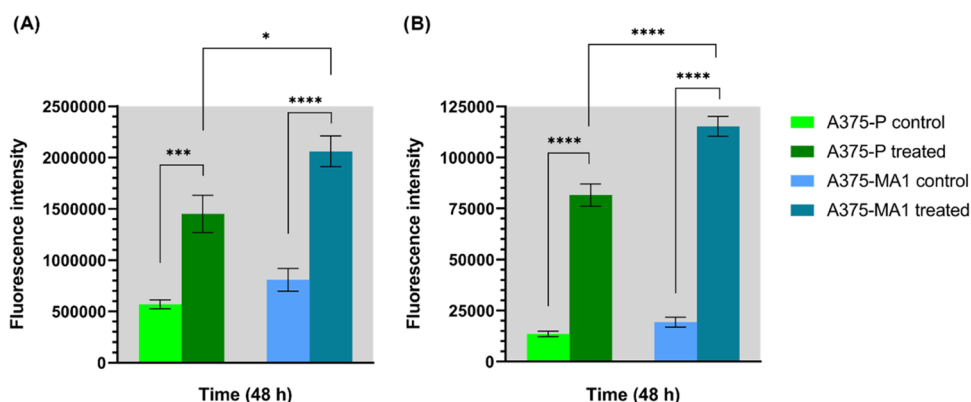

Figure 6. ROS generation levels in melanoma 3D models treated with nanoparticles for 48 h: (A) DCFDA assay; (B) MitoSOX assay.

spheroids had formed by day 4 of the seeding, at which point the medium was replaced. The spheroid morphology was significantly different between the two different cell lines even though the cell numbers seeded for the formation of the spheroids were the same. The A375-P cells formed spheroids that were loosely packed, which is confirmed subsequently in Section 3.7. In contrast, the A375-MA1 cells formed smaller, more rounded, and more tightly packed spheroids. There also is a spherical boundary between the region of loosely packed surface and the more compact bulk, which suggests a clear distinction between these two.

Although the seeding densities were the same for both cell lines, the spheroids of the A375-MA1 cells were smaller and more densely packed than the spheroids of the A375-P cells.

There do not appear to be any reports that interpret the causes of formation for morphologies similar to those in Figure S2 (Supporting Information). Consequently, the differences in packing densities are assumed to derive from differences in growth rates and the greater communication/cooperation within the metastatic cancer cells and their aggression, which would draw the cells into greater proximity. Again, these microstructural features are confirmed in Section 3.7.

3.6. Therapeutic Activity of Theranostic Nanoparticles in 3D Models. The cell viabilities of the spheroids that were untreated or treated with nanoparticles were determined qualitatively using the live/dead staining technique. This involves the use of the dyes calcein AM and EthD-1, where the former stains live cells and the latter stains dead cells. The
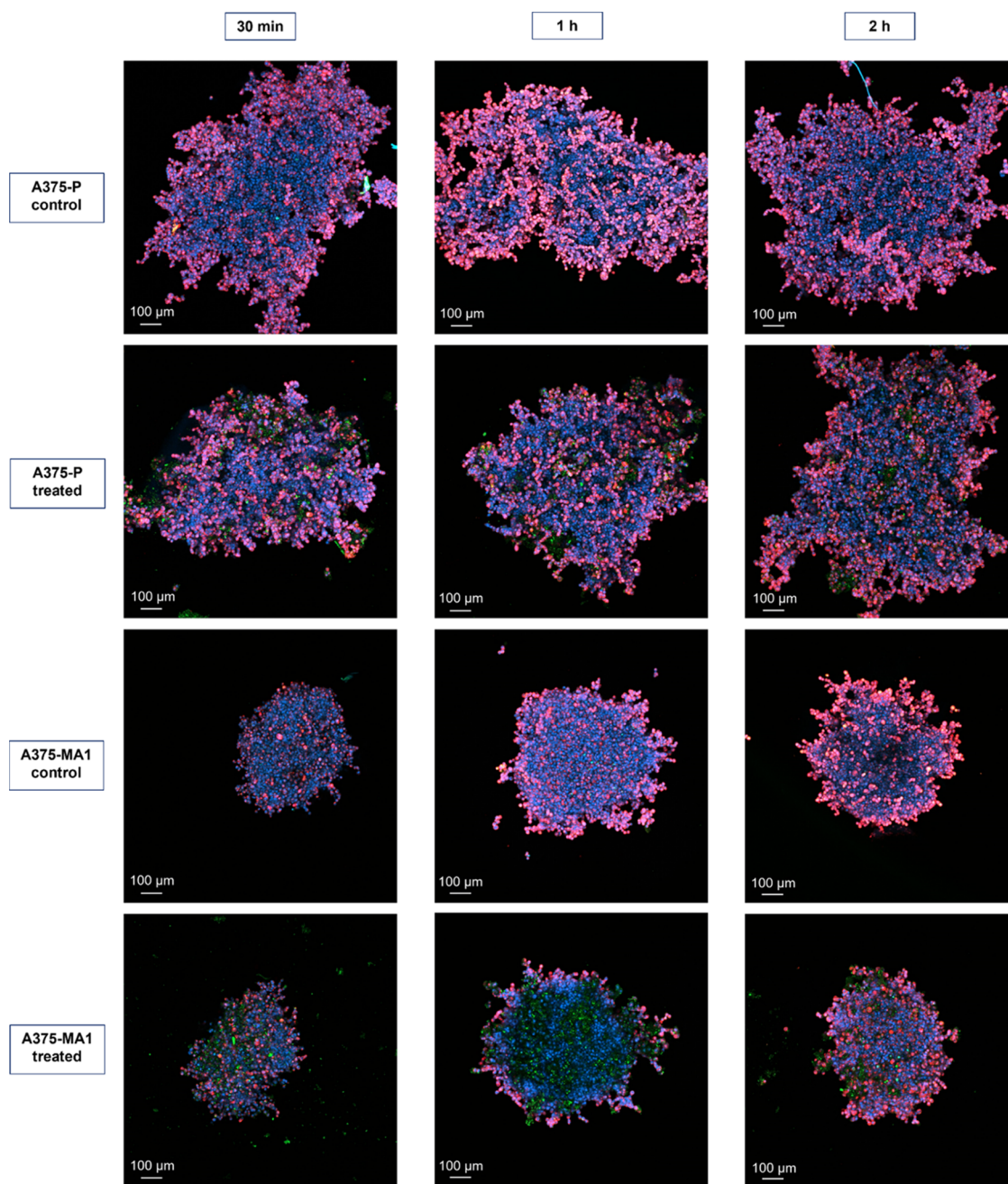
Figure 7. Confocal imaging of melanoma 3D models after treatment with EGFR-targeted nanoparticles for 30 min, 1 h, and 2 h.

principle is based on the esterase-mediated conversion of nonfluorescent calcein AM to green fluorescent calcein in live cells and the internalization of EthD-1 by dead cells while excluding live cells, where the associated red fluorescence derives from EthD-1 binding to nucleic acids. For this testing, unlike in all other testing, EGF-nanoceria particles without FITC labeling were used because both calcein and FITC produce green fluorescence, which would obscure the interpretation of the live cells.

Figure 5 shows the qualitative results after 48 h for the live/ dead staining by confocal imaging (maximum intensity projection of z-stacks). Although the green fluorescence of the control spheroids indicates the appearance of live and healthy cells, the red fluorescence of the parental and metastatic spheroids indicates unambiguous cell death. As the analyses are qualitative, the rates of cell death cannot be

determined and hence the data are indicative of the therapeutic performance of nanoceria on both parental and metastatic spheroids.

The therapeutic activity of the nanoparticles was demonstrated further by determining the ROS generation capability of nanoparticles upon uptake by the spheroids. Figure 6 shows the ROS generation levels of spheroids treated with nanoparticles at 48 h by DCFDA assay and MitoSOX assay. These data reveal that the ROS generation levels detected by both assays were greater for the treated spheroids relative to the untreated spheroids and that the ROS generation levels for the metastatic spheroids were greater than those for the parental spheroids.

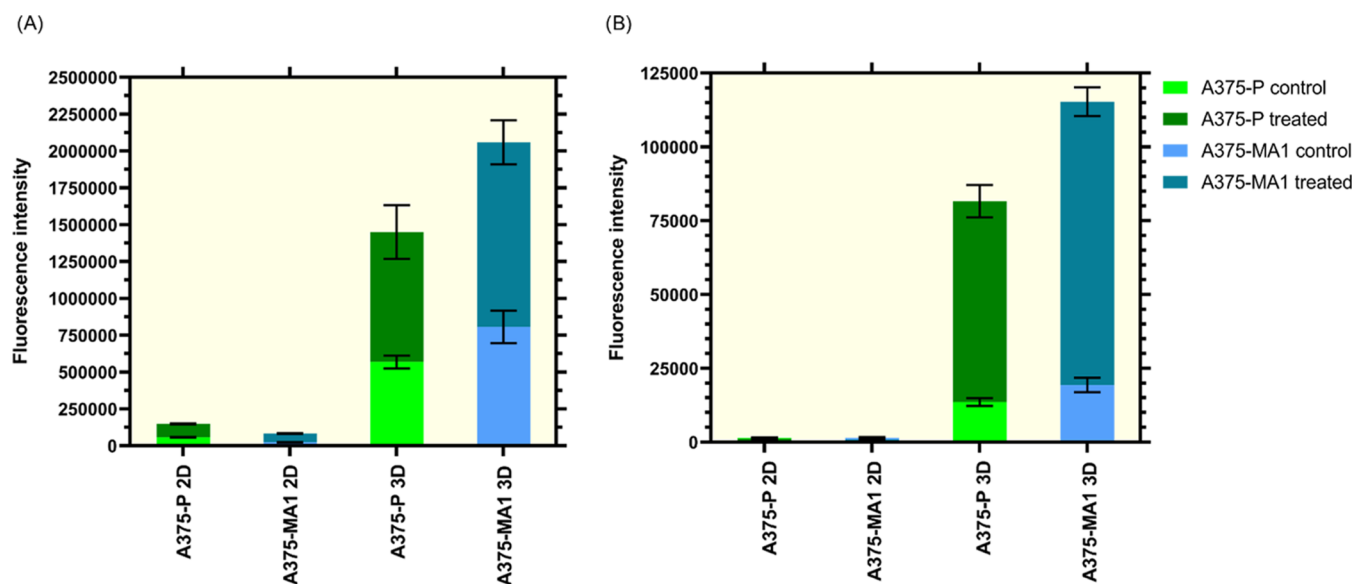The following key observations and conclusions about the 3D models can be made:

(A)

(B)

Figure 8. Comparison of ROS generation levels in melanoma 2D and 3D models treated with nanoparticles for 48 h: (A) DCFDA assay; (B) MitoSOX assay.

1. There is a considerable increase in the generation of the ROS H_2O_2 and $^\bullet OH$ detected by the DCFDA assay for both the parental and metastatic spheroids treated with nanoparticles. Thus, the ceria nanoparticles are enhancing the oxidative stress from ROS generation.

2. Despite the general slower growth rate of the metastatic cells compared to that of the parental cells (Sections 3.2 and 3.3), the basal levels of H_2O_2 and $^\bullet OH$ were higher for the metastatic spheroids compared to those of the parental spheroids. This is attributed to the more compact microstructure, which is assumed to enhance communication/cooperation within the metastatic cancer cells and their aggression (Section 3.5).

3. For the mitochondrial ROS testing by the MitoSOX assay, the data show that the ceria nanoparticle treatment increased the generation of $^\bullet O^{2-}$ for both the parental and metastatic spheroids. Thus, the ceria nanoparticles are capable of inducing mitochondrial oxidative stress for both types of spheroids.

4. Again, despite the general slower growth rate of the metastatic cells compared to that of the parental cells (Sections 3.2 and 3.3), the basal levels of $^\bullet O^{2-}$ were higher for the metastatic spheroids compared to those of the parental spheroids. This again is attributed to the more compact microstructure.

5. In summary, the preceding data indicate that the oxidative stress from the ROS generation induced by nanoceria is greater in the metastatic melanoma spheroids than the parental melanoma spheroids. These ROS levels are in addition to the basal ROS that are generated by the cells themselves, as indicated by the controls. In such ROS-mediated situations, cell death is induced when the sum of these ROS levels exceeds the cytotoxic levels.

3.7. Diagnostic Activity of Theranostic Nanoparticles in 3D Models. The diagnostic activities of the theranostic nanoparticles are further confirmed in the 3D models at the 30 min, 1 h, and 2 h time points, as demonstrated by treating the spheroids with nanoparticles functionalized with EGF (FITC-

tagged) and imaging their internalization using confocal microscopy (maximum intensity projection of z-stacks), as shown in Figure 7. The images confirm the differences in homogeneity, packing, and associated cell proximity mentioned in Section 3.5. In common with the 2D models, the detection of the green fluorescent nanoceria, even by 30 min, that are targeted at EGFR demonstrated the diagnostic activity of the nanoparticles on the EGFR-positive melanoma spheroids of both parental and metastatic cell lines.

3.8. Comparative Analysis of 2D and 3D Models. Comparative analysis of the therapeutic efficiency of nanoceria in 2D and 3D melanoma using ROS generation levels reveals the following in Figure 8, which is a composite of the individual data in Figures 2b and 6:

1. The ROS generation levels follow significantly different trends in 2D and 3D tumor models, where the latter is over an order a magnitude greater than that of the former for both cellular and mitochondrial ROS.

2. The respective fluorescence intensities of the DCFDA assay from cellular ROS production were ~150,000 and ~85,000 for the treated parental and metastatic 2D models. These respective levels also increased over an order of magnitude to ~1,600,000 and ~2,250,000 for the 3D treated models.

3. The respective fluorescence intensities of the MitoSOX assay from mitochondria-mediated ROS production were effectively absent in the 2D models (similar to blank values), but the ROS levels were very high in the 3D models, being ~90,000 and ~120,000 for the treated parental and metastatic 3D models, respectively.

4. The differences exhibited by these two models are consistent with those observed for other cell types.[53] As mentioned in the Section 1, these differences have been attributed to the limitations of the 2D models, which involve alteration of cell phenotype, polarity, and mode of division. Further, the 3D spheroidal microstructures are more representative of actual tumor masses and other *in vivo* conditions, including cell−cell and cell−environment interactions.

5. Although the comparative cell counts for 2D and 3D are unknown, it is surprising that the ROS levels of the 3D models are greater than those of the 2D models and the former is compact volumetric, and the latter is more exposed areal. This suggests that, despite the compact microstructure of the spheroids, the nanoparticle penetration, which is driven by the EGFR targeting, is effective.

6. Both the cellular and mitochondrial ROS levels were observed to be significantly higher for the treated metastatic models compared to those of the parental models. This is attributed to the higher expression levels of the former, which is confirmed by the cellular uptake levels quantified in the 2D models (Figure 3).

7. The preceding data suggest that the interpretation of the therapeutic effects of drugs based on 2D models alone risk leading to misleading conclusions.

8. Regardless, 2D models have the capacity to provide preliminary guidance in the performance of both diagnostic and therapeutic agents.

4. SUMMARY AND CONCLUSIONS

Functionalization of nanoceria with the negatively charged protein EGF tagged with FITC yielded negatively charged nanoparticles, as shown by the DLS results. The therapeutic activity of ceria-based theranostic nanoparticles in parental and metastatic 2D models revealed similar therapeutic performance levels. The ROS generation levels, which indicate direct measures of the therapeutic performance of nanoceria, were measured. There were significant enhancements in the generation of cellular ROS species, H_2O_2, and $^\bullet OH$, as measured by the DCFDA assay on both parental and metastatic 2D models. In contrast, there was no significant generation of the mitochondrial ROS species $^\bullet O_2^-$, as measured by the MitoSOX assay. Although this indicates an absence of mitochondrial oxidative stress, this was disproved by the 3D models. The cellular uptake of nanoparticles was significantly higher (by >50%) for the treated metastatic 2D models compared to that for the parental models. This is attributed to the higher level of EGFR expression in metastatic melanoma, which facilitated greater uptake of nanoparticles through EGFR-mediated endocytosis. Confocal imaging studies confirmed the diagnostic activity of nanoparticles as they could be imaged successfully after treatment and subsequent washing of residual nanoparticles. Nanoparticles were observed to interact with the cells at the time point studied (30 min), as revealed by their contact with the cells or their partial internalization by the cells.

The 3D parental and metastatic spheroids generated exhibited significant differences in their appearances and packing densities. These differences were assumed to be derived from the differences in growth rates and the greater communication/cooperation within the metastatic cancer cells and their aggression. The live-dead imaging of the nanoparticle-treated 3D models demonstrated significant cell death in the treated spheroids. The therapeutic activity of the nanoparticles was confirmed further by measuring the ROS levels in the treated spheroids and these data revealed enhanced oxidative stress for both the parental and metastatic models. H_2O_2 and $^\bullet OH$, which are indicative of cellular oxidative stress, and $^\bullet O_2^-$, which is indicative of mitochondrial oxidative stress, were enhanced significantly in both the parental and metastatic spheroids treated with nanoparticles. Elevation in the levels of all three ROS species was significantly higher for the treated metastatic spheroids compared to that for the parental spheroids, thus indicating improved therapeutic performance in metastatic melanoma. Despite the general slow growth rate of the metastatic cells, higher basal levels of all three ROS species were observed in the untreated control spheroids of the metastatic cell line in comparison to that of the parental cell line. The aggressiveness and the compact microstructure of metastatic spheroids and their associated enhanced communication/cooperation were considered to cause the higher basal levels.

The diagnostic activity of the nanoparticles in the 3D models was confirmed by the successful detection of fluorescent nanoparticles using confocal imaging at all time points studied. This result is similar to that observed for the 2D models.

A comparative analysis of the data generated from the 2D and 3D models was performed and this revealed significantly different trends for ROS generation. The cellular ROS generation levels increased by over an order of magnitude for the treated 3D models relative to those of the 2D models. The mitochondrial ROS levels also were elevated significantly in the treated 3D models relative to their controls for both parental and metastatic cells. In this case, the 2D models revealed no apparent effect on the mitochondria. This significant difference between the 2D and 3D data sets is attributed to the limitations of the 2D models, which involve alteration of cell phenotype, polarity, and mode of division in 2D cultures.

Finally, the present work demonstrates the suitability of the nanoceria-based theranostic formulation for the management of melanoma. Further, it can provide an excellent therapeutic strategy for the treatment of EGFR-positive metastatic melanomas, thereby improving the survival rates of patients, where survival rates decrease considerably after tumor metastasis.

■ ASSOCIATED CONTENT

Ⓢ Supporting Information

The Supporting Information is available free of charge at https://pubs.acs.org/doi/10.1021/acsbiomaterials.2c01258.

> DLS data for APTES-nanoceria and FITC-EGF-nanoceria (Table S1); cellular uptake levels of nanoceria by parental and metastatic cells (Table S2); DLS analyses of APTES-nanoceria and FITC-EGF-nanoceria (Figure S1); and images of untreated spheroids for parental and metastatic melanoma (Figure S2) (PDF)

■ AUTHOR INFORMATION

Corresponding Author

Kochurani K. Johnson − *School of Materials Science and Engineering, Faculty of Science, UNSW Sydney, Sydney, NSW 2052, Australia;* ⓞ orcid.org/0000-0002-4635-714X; Email: k.kandamkulathyjohnson@unsw.edu.au

Authors

Chantal Kopecky − *Australian Centre for NanoMedicine, School of Chemistry, Faculty of Science, UNSW Sydney, Sydney, NSW 2052, Australia*

Pramod Koshy − *School of Materials Science and Engineering, Faculty of Science, UNSW Sydney, Sydney, NSW 2052, Australia*

Yiling Liu − *Australian Centre for NanoMedicine, School of Chemistry, Faculty of Science, UNSW Sydney, Sydney, NSW 2052, Australia*

Michelle Devadason − *Translational Cancer Metabolism Laboratory, School of Medical Sciences and Prince of Wales Clinical School, Faculty of Medicine and Health, UNSW Sydney, Sydney, NSW 2052, Australia*

Jeff Holst − *Translational Cancer Metabolism Laboratory, School of Medical Sciences and Prince of Wales Clinical School, Faculty of Medicine and Health, UNSW Sydney, Sydney, NSW 2052, Australia*

Kristopher A. Kilian − *School of Materials Science and Engineering, Faculty of Science, UNSW Sydney, Sydney, NSW 2052, Australia; Australian Centre for NanoMedicine, School of Chemistry, Faculty of Science, UNSW Sydney, Sydney, NSW 2052, Australia;* orcid.org/0000-0002-8963-9796

Charles C. Sorrell − *School of Materials Science and Engineering, Faculty of Science, UNSW Sydney, Sydney, NSW 2052, Australia;* orcid.org/0000-0002-1915-657X

Complete contact information is available at:
https://pubs.acs.org/10.1021/acsbiomaterials.2c01258

Author Contributions

K.K.J.: conceptualization; experimental design; nanoparticle synthesis and characterization; cell viability, ROS generation, and cellular uptake level measurement assays; confocal imaging; data analysis; writing of initial draft of manuscript. C.K.: assistance with experimental design; assistance with spheroid generation; analysis and processing of confocal imaging data; reviewing and editing of final draft of manuscript. P.K.: data analysis support; reviewing and editing of initial and final drafts of manuscript. Y.L.: DLS analysis; writing of DLS analysis section. M.D.: Western blotting. J.H.: reviewing and editing of final draft of manuscript. K.A.K.: assistance with experimental design; assistance with experimentation; data analysis support; reviewing and editing of final draft of manuscript. C.C.S.: project supervision; funding acquisition; data analysis; reviewing and editing of all drafts of manuscript.

Notes

The authors declare no competing financial interest.

■ REFERENCES

(1) Johnson, K. K.; Koshy, P.; Yang, J. L.; Sorrell, C. C. Preclinical Cancer Theranostics—From Nanomaterials to Clinic: The Missing Link. *Adv. Funct. Mater.* **2021**, *31*, No. 2104199.

(2) Kelkar, S. S.; Reineke, T. M. Theranostics: combining imaging and therapy. *Bioconjugate Chem.* **2011**, *22*, 1879−1903.

(3) Jeelani, S.; Reddy, R. C. J.; Maheswaran, T.; Asokan, G.; Dany, A.; Anand, B. Theranostics: A treasured tailor for tomorrow. *J. Pharm. BioAllied Sci.* **2014**, *6*, S6.

(4) Li, X.; Kim, J.; Yoon, J.; Chen, X. Cancer-associated, stimuli-driven, turn on theranostics for multimodality imaging and therapy. *Adv. Mater.* **2017**, *29*, No. 1606857.

(5) Thakur, N.; Manna, P.; Das, J. Synthesis and biomedical applications of nanoceria, a redox active nanoparticle. *J. Nanobiotechnol.* **2019**, *17*, No. 84.

(6) Saifi, M. A.; Seal, S.; Godugu, C. Nanoceria, the versatile nanoparticles: Promising biomedical applications. *J. Controlled Release* **2021**, *338*, 164−189.

(7) Thakur, N.; Das, J.; Sil, P. C. Emerging Role of Redox-Active Nanoceria in Cancer Therapeutics via Oxidative Stress. *Handbook of Oxidative Stress in Cancer: Therapeutic Aspects*; Springer, 2021; pp 1−23.

(8) Corsi, F.; Caputo, F.; Traversa, E.; Ghibelli, L. Not only redox: the multifaceted activity of cerium oxide nanoparticles in cancer prevention and therapy. *Front. Oncol.* **2018**, *8*, No. 309.

(9) Mehmood, R.; Ariotti, N.; Yang, J. L.; Koshy, P.; Sorrell, C. C. pH-responsive morphology-controlled redox behavior and cellular uptake of nanoceria in fibrosarcoma. *ACS Biomater. Sci. Eng.* **2018**, *4*, 1064−1072.

(10) Dutta, D.; Mukherjee, R.; Ghosh, S.; Patra, M.; Mukherjee, M.; Basu, T. Cerium Oxide Nanoparticles as Antioxidant or Pro-oxidant Agents. *ACS Appl. Nano Mater.* **2022**, *5*, 1690.

(11) Dewaele, M.; Maes, H.; Agostinis, P. ROS-mediated mechanisms of autophagy stimulation and their relevance in cancer therapy. *Autophagy* **2010**, *6*, 838−854.

(12) Wang, J.; Yi, J. Cancer cell killing via ROS: to increase or decrease, that is the question. *Cancer Biol. Ther.* **2008**, *7*, 1875−1884.

(13) Basak, D.; Arrighi, S.; Darwiche, Y.; Deb, S. Comparison of anticancer drug toxicities: paradigm shift in adverse effect profile. *Life* **2022**, *12*, No. 48.

(14) Torino, F.; Barnabei, A.; Paragliola, R.; Baldelli, R.; Appetecchia, M.; Corsello, S. M. Thyroid dysfunction as an unintended side effect of anticancer drugs. *Thyroid* **2013**, *23*, 1345−1366.

(15) Carr, C.; Ng, J.; Wigmore, T. The side effects of chemotherapeutic agents. *Curr. Anaesth. Crit. Care* **2008**, *19*, 70−79.

(16) Perrino, C.; Schiattarella, G.; Magliulo, F.; Ilardi, F.; Carotenuto, G.; Gargiulo, G.; Serino, F.; Ferrone, M.; Scudiero, F.; Carbone, A.; et al. Cardiac side effects of chemotherapy: state of art and strategies for a correct management. *Curr. Vasc. Pharmacol.* **2014**, *12*, 106−116.

(17) Ko, Y. J.; Kim, W. J.; Kim, K.; Kwon, I. C. Advances in the strategies for designing receptor-targeted molecular imaging probes for cancer research. *J. Controlled Release* **2019**, *305*, 1−17.

(18) Brennan, M.; Lim, B.The Actual Role of Receptors as Cancer Markers, Biochemical and Clinical Aspects: Receptors in Breast Cancer. *Advances in Cancer Biomarkers*; Springer, 2015; pp 327−337.

(19) Lappano, R.; Maggiolini, M. GPCRs and cancer. *Acta Pharmacol. Sin.* **2012**, *33*, 351−362.

(20) Wu, P.-H.; Opadele, A. E.; Onodera, Y.; Nam, J.-M. Targeting integrins in cancer nanomedicine: applications in cancer diagnosis and therapy. *Cancers* **2019**, *11*, No. 1783.

(21) Sigismund, S.; Avanzato, D.; Lanzetti, L. Emerging functions of the EGFR in cancer. *Mol. Oncol.* **2018**, *12*, 3−20.

(22) Ledermann, J.; Canevari, S.; Thigpen, T. Targeting the folate receptor: diagnostic and therapeutic approaches to personalize cancer treatments. *Ann. Oncol.* **2015**, *26*, 2034−2043.

(23) Wang, M.; Thanou, M. Targeting nanoparticles to cancer. *Pharmacol. Res.* **2010**, *62*, 90−99.

(24) Van Dam, G. M.; Themelis, G.; Crane, L. M.; Harlaar, N. J.; Pleijhuis, R. G.; Kelder, W.; Sarantopoulos, A.; De Jong, J. S.; Arts, H. J.; Van Der Zee, A. G.; et al. Intraoperative tumor-specific

fluorescence imaging in ovarian cancer by folate receptor-α targeting: first in-human results. *Nat. Med.* **2011**, *17*, 1315−1319.

(25) Zhang, S.; Shao, P.; Bai, M. In vivo type 2 cannabinoid receptor-targeted tumor optical imaging using a near infrared fluorescent probe. *Bioconjugate Chem.* **2013**, *24*, 1907−1916.

(26) Pewklang, T.; Chansaenpak, K.; Lai, R.-Y.; Noisa, P.; Kamkaew, A. Aza-BODIPY probe for selective visualization of cyclooxygenase-2 in cancer cells. *RSC Adv.* **2019**, *9*, 13372−13377.

(27) Qiao, J.; Dong, P.; Mu, X.; Qi, L.; Xiao, R. Folic acid-conjugated fluorescent polymer for up-regulation folate receptor expression study via targeted imaging of tumor cells. *Biosens. Bioelectron.* **2016**, *78*, 147−153.

(28) Zhang, Y.; Li, S.; Zhang, H.; Xu, H. Design and application of receptor-targeted fluorescent probes based on small molecular fluorescent dyes. *Bioconjugate Chem.* **2021**, *32*, 4−24.

(29) Suganya S, A. A.; Kochurani, K. J.; Nair, M. G.; Louis, J. M.; Sankaran, S.; Rajagopal, R.; Kumar, K. S.; Abraham, P.; Balagopal, P. G.; Sebastian, P.; et al. TM1-IR680 peptide for assessment of surgical margin and lymph node metastasis in murine orthotopic model of oral cancer. *Sci. Rep.* **2016**, *6*, No. 36726.

(30) Aparicio-Blanco, J.; Torres-Suárez, A.-I. Towards tailored management of malignant brain tumors with nanotheranostics. *Acta Biomater.* **2018**, *73*, 52−63.

(31) Fang, H.; Cavaliere, A.; Li, Z.; Huang, Y.; Marquez-Nostra, B. Preclinical advances in theranostics for the different molecular subtypes of breast cancer. *Front. Pharmacol.* **2021**, *12*, No. 627693.

(32) Zhou, H.; Qian, W.; Uckun, F. M.; Wang, L.; Wang, Y. A.; Chen, H.; Kooby, D.; Yu, Q.; Lipowska, M.; Staley, C. A.; et al. IGF1 receptor targeted theranostic nanoparticles for targeted and image-guided therapy of pancreatic cancer. *ACS Nano* **2015**, *9*, 7976−7991.

(33) Sun, T.; Zhang, G.; Ning, T.; Chen, Q.; Chu, Y.; Luo, Y.; You, H.; Su, B.; Li, C.; Guo, Q.; Versatile, A. Theranostic Platform for Colorectal Cancer Peritoneal Metastases: Real-Time Tumor-Tracking and Photothermal-Enhanced Chemotherapy. *Adv. Sci.* **2021**, *8*, No. 2102256.

(34) Del Vecchio, S.; Zannetti, A.; Fonti, R.; Pace, L.; Salvatore, M. Nuclear imaging in cancer theranostics. *Q. J. Nucl. Med. Mol. Imaging* **2007**, *51*, 152−163.

(35) Gargiulo, S.; Albanese, S.; Mancini, M. State-of-the-art preclinical photoacoustic imaging in oncology: recent advances in cancer theranostics. *Contrast Media Mol. Imaging* **2019**, *2019*, 1−24.

(36) Anani, T.; Rahmati, S.; Sultana, N.; David, A. E. MRI-traceable theranostic nanoparticles for targeted cancer treatment. *Theranostics* **2021**, *11*, 579.

(37) Alibolandi, M.; Abnous, K.; Sadeghi, F.; Hosseinkhani, H.; Ramezani, M.; Hadizadeh, F. Folate receptor-targeted multimodal polymersomes for delivery of quantum dots and doxorubicin to breast adenocarcinoma: in vitro and in vivo evaluation. *Int. J. Pharm.* **2016**, *500*, 162−178.

(38) Wang, S.; Li, C.; Qian, M.; Jiang, H.; Shi, W.; Chen, J.; Lächelt, U.; Wagner, E.; Lu, W.; Wang, Y.; Huang, R. Augmented glioma-targeted theranostics using multifunctional polymer-coated carbon nanodots. *Biomaterials* **2017**, *141*, 29−39.

(39) Wu, J.; Zhou, Y.; Li, S.; Qu, D.; Zhu, W.-H.; Tian, H. Real-time near-infrared bioimaging of a receptor-targeted cytotoxic dendritic theranostic agent. *Biomaterials* **2017**, *120*, 1−10.

(40) Satpathy, M.; Wang, L.; Zielinski, R. J.; Qian, W.; Wang, Y. A.; Mohs, A. M.; Kairdolf, B. A.; Ji, X.; Capala, J.; Lipowska, M.; et al. Targeted drug delivery and image-guided therapy of heterogeneous ovarian cancer using her2-targeted theranostic nanoparticles. *Theranostics* **2019**, *9*, 778.

(41) Yang, X.; Wang, Z.; Zhang, F.; Zhu, G.; Song, J.; Teng, G.-J.; Niu, G.; Chen, X. Mapping sentinel lymph node metastasis by dual-probe optical imaging. *Theranostics* **2017**, *7*, 153.

(42) Domingues, B.; Lopes, J. M.; Soares, P.; Pópulo, H. Melanoma treatment in review. *ImmunoTargets Ther.* **2018**, *7*, 35.

(43) Gogas, H.; Dummer, R.; Ascierto, P. A.; Arance, A.; Mandalà, M.; Liszkay, G.; Garbe, C.; Schadendorf, D.; Krajsová, I.; Gutzmer, R.; et al. Quality of life in patients with BRAF-mutant melanoma

receiving the combination encorafenib plus binimetinib: Results from a multicentre, open-label, randomised, phase III study (COLUMBUS). *Eur. J. Cancer* **2021**, *152*, 116−128.

(44) Davis, L. E.; Shalin, S. C.; Tackett, A. J. Current state of melanoma diagnosis and treatment. *Cancer Biol. Ther.* **2019**, *20*, 1366−1379.

(45) Sondermann, W.; Zimmer, L.; Schadendorf, D.; Roesch, A.; Klode, J.; Dissemond, J. Initial misdiagnosis of melanoma located on the foot is associated with poorer prognosis. *Medicine* **2016**, *95*, No. e4332.

(46) Kozar, I.; Margue, C.; Rothengatter, S.; Haan, C.; Kreis, S. Many ways to resistance: How melanoma cells evade targeted therapies. *Biochim. Biophys. Acta, Rev. Cancer* **2019**, *1871*, 313−322.

(47) Mendelsohn, J.; Baselga, J. Status of epidermal growth factor receptor antagonists in the biology and treatment of cancer. *J. Clin. Oncol.* **2003**, *21*, 2787−2799.

(48) Lee, K. H.; Suh, H. Y.; Lee, M. W.; Lee, W. J.; Chang, S. E. Prognostic Significance of Epidermal Growth Factor Receptor Expression in Distant Metastatic Melanoma from Primary Cutaneous Melanoma. *Ann. Dermatol.* **2021**, *33*, 432.

(49) Teutschbein, J.; Haydn, J. M.; Samans, B.; Krause, M.; Eilers, M.; Schartl, M.; Meierjohann, S. Gene expression analysis after receptor tyrosine kinase activation reveals new potential melanoma proteins. *BMC Cancer* **2010**, *10*, No. 386.

(50) Sriramarao, P.; Bourdon, M. A. Melanoma cell invasive and metastatic potential correlates with endothelial cell reorganization and tenascin expression. *Endothelium* **1996**, *4*, 85−97.

(51) Chandrasekaran, S.; Giang, U.-B. T.; Xu, L.; DeLouise, L. A. In vitro assays for determining the metastatic potential of melanoma cell lines with characterized in vivo invasiveness. *Biomed. Microdevices* **2016**, *18*, No. 89.

(52) Bédard, P.; Gauvin, S.; Ferland, K.; Caneparo, C.; Pellerin, È.; Chabaud, S.; Bolduc, S. Innovative human three-dimensional tissue-engineered models as an alternative to animal testing. *Bioengineering* **2020**, *7*, No. 115.

(53) Kapałczyńska, M.; Kolenda, T.; Przybyła, W.; Zajączkowska, M.; Teresiak, A.; Filas, V.; Ibbs, M.; Bliźniak, R.; Łuczewski, Ł.; Lamperska, K. 2D and 3D cell cultures−a comparison of different types of cancer cell cultures. *Arch. Med. Sci.* **2018**, *14*, 910.

(54) Mehmood, R.; Wang, X.; Koshy, P.; Yang, J. L.; Sorrell, C. C. Engineering oxygen vacancies through construction of morphology maps for bio-responsive nanoceria for osteosarcoma therapy. *CrystEngComm* **2018**, *20*, 1536−1545.

(55) Sun, M.; Wang, T.; Li, L.; Li, X.; Zhai, Y.; Zhang, J.; Li, W. The application of inorganic nanoparticles in molecular targeted cancer therapy: EGFR targeting. *Front. Pharmacol.* **2021**, *12*, No. 702445.

(56) da Silva Santos, E.; Nogueira, K. A. B.; Fernandes, L. C. C.; Martins, J. R. P.; Reis, A. V. F.; Neto, J. d. B. V.; da Silva Júnior, I. J.; Pessoa, C.; Petrilli, R.; Eloy, J. O. EGFR targeting for cancer therapy: Pharmacology and immunoconjugates with drugs and nanoparticles. *Int. J. Pharm.* **2021**, *592*, No. 120082.

(57) Gao, M.; Su, H.; Lin, G.; Li, S.; Yu, X.; Qin, A.; Zhao, Z.; Zhang, Z.; Tang, B. Z. Targeted imaging of EGFR overexpressed cancer cells by brightly fluorescent nanoparticles conjugated with cetuximab. *Nanoscale* **2016**, *8*, 15027−15032.

(58) Kandamkulathy Johnson, K. *Nanoceria for ROS-Mediated Cancer Therapy: A Receptor-Targeted Theranostic Approach*; UNSW Sydney, 2022.

(59) Sorrell, C. C.; Taib, H.; Palmer, T. C.; Peng, F.; Xia, Z.; Wei, M.Hydroxyapatite and Other Biomedical Coatings By Electrophoretic Deposition. *Biological and Biomedical Coatings Handbook: Processing and Characterization*; CRC Press, 2011; pp 81−137.

(60) Yamada, K.; Yoshii, S.; Kumagai, S.; Fujiwara, I.; Nishio, K.; Okuda, M.; Matsukawa, N.; Yamashita, I. High-density and highly surface selective adsorption of protein−nanoparticle complexes by controlling electrostatic interaction. *Jpn. J. Appl. Phys.* **2006**, *45*, 4259.

(61) Kim, N. A.; Lim, D. G.; Lim, J. Y.; Kim, K. H.; Jeong, S. H. Fundamental analysis of recombinant human epidermal growth factor

in solution with biophysical methods. *Drug Dev. Ind. Pharm.* **2015**, *41*, 300−306.

(62) Staibano, S.; Pepe, S.; Soyer, P.; Argenziano, G.; Somma, P.; Mansueto, G.; Mascolo, M.; Bianco, A.; Laus, G.; De Rosa, G. Epidermal growth factor receptor (EGFR) expression in cutaneous melanoma: A possible role as prognostic marker. *Melanoma Res.* **2004**, *14*, S26.

(63) Jiménez-García, G.; de Lasa, H.; Quintana-Solórzano, R.; Maya-Yescas, R. Catalyst activity decay due to pore blockage during catalytic cracking of hydrocarbons. *Fuel* **2013**, *110*, 89−98.

(64) Haider, M. R.; Jiang, W.-L.; Han, J.-L.; Sharif, H. M. A.; Ding, Y.-C.; Cheng, H.-Y.; Wang, A.-J. In-situ electrode fabrication from polyaniline derived N-doped carbon nanofibers for metal-free electro-Fenton degradation of organic contaminants. *Appl. Catal., B* **2019**, *256*, No. 117774.

(65) Liu, W.; Tkatchenko, A.; Scheffler, M. Modeling adsorption and reactions of organic molecules at metal surfaces. *Acc. Chem. Res.* **2014**, *47*, 3369−3377.

(66) Thomas, N.; Dionysiou, D. D.; Pillai, S. C. Heterogeneous Fenton catalysts: A review of recent advances. *J. Hazard. Mater.* **2021**, *404*, No. 124082.

(67) Zhang, J.; Lou, X.; Jin, L.; Zhou, R.; Liu, S.; Xu, N.; Liao, D. J. Necrosis, and then stress induced necrosis-like cell death, but not apoptosis, should be the preferred cell death mode for chemotherapy: clearance of a few misconceptions. *Oncoscience* **2014**, *1*, 407.

(68) Ölander, M.; Handin, N.; Artursson, P. Image-based quantification of cell debris as a measure of apoptosis. *Anal. Chem.* **2019**, *91*, 5548−5552.

(69) Gao, Y.; Chen, K.; Ma, J.-l.; Gao, F. Cerium oxide nanoparticles in cancer. *OncoTargets Ther.* **2014**, *7*, 835.

(70) Li, Y.; Yang, J.; Sun, X. Reactive oxygen species-based nanomaterials for cancer therapy. *Front. Chem.* **2021**, *9*, No. 650587.

(71) Wileman, T.; Harding, C.; Stahl, P. Receptor-mediated endocytosis. *Biochem. J.* **1985**, *232*, 1.

(72) Sanders, J. M.; Wampole, M. E.; Thakur, M. L.; Wickstrom, E. Molecular determinants of epidermal growth factor binding: a molecular dynamics study. *PLoS One* **2013**, *8*, No. e54136.

(73) Vieira, A. V.; Lamaze, C.; Schmid, S. L. Control of EGF receptor signaling by clathrin-mediated endocytosis. *Science* **1996**, *274*, 2086−2089.